Out-of-plane motion of a thrust sheet during along-strike propagation of a thrust ramp: a distinct-element approach

Luther M. Strayer[*], John Suppe

Department of Geosciences, Guyot Hall, Princeton University, Princeton, NJ 08544, USA

Abstract

Using a 3D distinct-element mechanical modeling program, we examined the nature and magnitude of out-of-plane motion during along-strike propagation of a simple thrust ramp and attendant fault-related folding. Our numerical model was composed of about 83,000 spherical elastic particles that were bonded together to create an initial solid numerical rock mass, capable of macroscopic fracture and faulting in response to displacement loading. The algorithim is fully dynamic and as such allowed for the storage and sudden release of elastic strain energy in the form of seismic events.

We induced progressive along-strike fault-growth and attendant non-cylindrical fold development by varying the along-strike friction within a seeded, planar zone of weakness within the aggregate, a zone that was to become the fault. The result was a well-developed, plunging ramp anticline that grew in amplitude and along-strike length as the macroscopic fault propagated from lower to higher friction regions. Lateral fault propagation was relatively rapid compared with shortening, with a ratio of thrust displacement-to-propagation length (K) of 6.5%.

Incremental motion of the particles reflected episodic slip at both the laterally propagating fault-tip and along the existing fault. These episodes were characterized by local clusters of outward radiating velocity vectors that propagated at seismic velocities, marking the model equivalents of earthquakes.

The finite displacement vectors in the hanging wall were approximately parallel to the far-field transport direction, with a strike-parallel component that ranged from one to two orders of magnitude less than the strike-perpendicular component. Furthermore, about two-thirds of the particles had strike-parallel motion in the direction of fault propagation and fold plunge. Because the far-field, shortening boundary conditions were uniformly perpendicular to fault strike, this component of motion in the plunge direction was apparently due to a topographically-induced, plunge-parallel shear stress. The along-strike motion involved slip on the main fault as well as transient strike slip on minor vertical, sometimes conjugate zones, apparently induced by the increased topographic load. © 2002 Published by Elsevier Science Ltd.

Keywords: Out-of-plane motion; Thrust sheet; Thrust ramp

1. Introduction

For years it has been possible to describe the 3D structure of fold-and-thrust belts mainly by the construction of closely spaced serial cross-sections because of the approximately cylindrical geometry of many structures (Stockwell, 1950; Dahlstrom, 1969; Wilkerson et al., 1991; Shaw et al., 1994; Poblet et al., 1998; Rowen and Linares, 2000). However, out-of-plane motion is typically not taken into account by these methods. More recently, with the improved quality and availability of 3D seismic reflection surveys, direct mapping of deformed volumes provides the geologist with a more accurate depiction of the true 3D geometry of complicated structures (e.g. Bilotti et al., 1998; Fermor, 1999; Rouby et al., 2000).

Similarly, numerical models of thrust systems have been mostly limited to two dimensions, simulating either the deformation at a single thrust ramp (e.g. Erickson, 1995; Erickson and Jamison, 1995; Strayer and Hudleston, 1997a; Allmendinger, 1998) or along an entire cross-sectional thrust system (e.g. Liu and Dixon, 1990; Strayer and Hudleston, 1997b). Three-dimensional modeling has been limited to pseudo-3D geometric methods (Wilkerson et al., 1991; Shaw et al., 1994; Poblet et al., 1998; Cristallini and Allmendinger, 1999; Rowen and Linares, 2000) or analog models (Liu and Dixon, 1991; Dixon and Liu, 1992; Dixon and Spratt, 1999), which allow first-order

* Corresponding author. Current address: Department of Geological Sciences, California State University, Hayward, Hayward, CA 94542, USA.

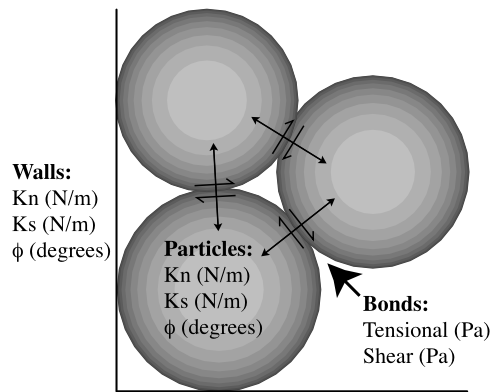*E-mail address:* lstrayer@csuhayward.edu (L.M. Strayer).

Fig. 1. Microscopic elements of the model. Model components include frictional, linear-elastic, spherical particles that act as springs in compression; frictional, elastic walls that are either fixed or velocity controlled; and contact bonds that resist tensional separation and shear displacement. Bonds are applied after the particles achieve static gravitational equilibrium, creating an initial solid that is capable of progressive fracture during loading. Particle size is determined by computational limitations and is varied about a mean radius of 50 m to prevent formation of hexagonal close-packed array. Kn and Ks are the particle and wall bulk and shear moduli, respectively. Particle and wall friction angle ϕ is simply a convenient representation of the critical ratio of shear to normal force required for a contact to slide.

thrust-belt kinematics to be studied. With recent improvements in computer processing speed and in 3D mechanical modeling software (e.g. Itasca, 1999b), we can now begin to construct 3D numerical models of thrust systems, with the goal of quantifying not only their kinematic evolution, but their mechanical development as well.

As an initial exploration of 3D mechanical numerical modeling of thrust systems, we constructed a relatively simple 3D model of a fault-related fold that formed by along-strike growth of a thrust fault from a seeded, planar zone of material weakness. By tracking material displacement, we hope to gain insight into the mechanisms and relative magnitudes of in-plane and out-of-plane material motion during thrust fault formation and along-strike fault growth.

2. The model

2.1. Modeling approach

Our 3D numerical model of a growing thrust fault and attendant folding has simple initial and boundary conditions. In effect, we created a numerical sandbox with elastic, frictional walls that contained elastic, self-gravitating frictional 'grains'. The size of the box and number of particles is limited by computer speed and memory. Deformation is induced by displacing one of the walls incrementally.

Our model is based on the *distinct-element method* (Cundall and Strack, 1979), which was developed originally to study the behavior and interaction of granular materials, but has been extended using particle bonds to study

problems in solid mechanics such as mine-site stability (Cundall, 1988), rock mechanics (Potyondy et al., 1996; Cundall, 2001), and seismicity associated with rock fracture (Hazzard et al., 1998; Young et al., 2000). The method also has been employed to study problems in structural geology in 2D, such as normal faulting (Saltzer and Pollard, 1991; Finch and McCloskey, 1996), fault gouge formation (Morgan, 1998), and the mechanical effects of syntectonic sedimentation on fold growth above a thrust ramp (Strayer et al., 1999a,b).

In spite of the fact that distinct-element models may be thought of as granular 'numerical sandboxes', the issues involved in comparing such models with geologic structures are substantially different from those of sandbox or other physical analog models. With physical models, you adjust the combination of size, physical properties, gravity and time to demonstrate that you have a reasonable analog based on dimensional analysis. In contrast, continuum and distinct-element numerical models are not 'scale models' in the sense of physical models. The arguments that must be made to say that we have an enlightened analog to geologic structures do not involve issues of 'scale' or significant dimensional analysis. In continuum or distinct-element numerical models, size, time and gravity are fixed to typical Earth values. The only adjustable or 'scale' parameters are constituitive properties in a continuum model or low-level particle properties in a distinct-element model. The arguments for analogy between earth structures and numerical models involve discussions of the combination of (1) physical properties and their spatial heterogeneity and (2) possible numerical artifacts of the numerical model that might subvert the physical properties, in relationship to (a) the general physical properties and (b) actual time-dependent, heterogeneous, and anisotropic physical properties of specific geologic structures.

2.2. The distinct-element method

The distinct-element method is based on the fundamental physics of Hertzian elastic, frictional particle interaction. We used the software PFC3D (Particle Flow Code in Three Dimensions; Itasca, 1999b), which employs the distinct-element method with the following assumptions: (1) particles are spherical and elastic; (2) contacts between particles occur over a vanishingly small area (i.e. at a point); (3) the magnitude of elastic particle 'overlap' of nominal radii is related to the contact force by a force-displacement law similar to linear springs that mimic the physics of Hertzian elastic spheres; and (4) tensional and shear bonds can exist between particles. Thus, individual particles act as linear-elastic springs in compression with cohesive contact bonding that acts in both shear and tension, and Coulomb frictional sliding that acts only along unbonded contacts (Fig. 1). Deformation of the bonded aggregate is induced by movement of elastic, frictional walls and/or by gravity. The bonded aggregate may produce realistic fractures and
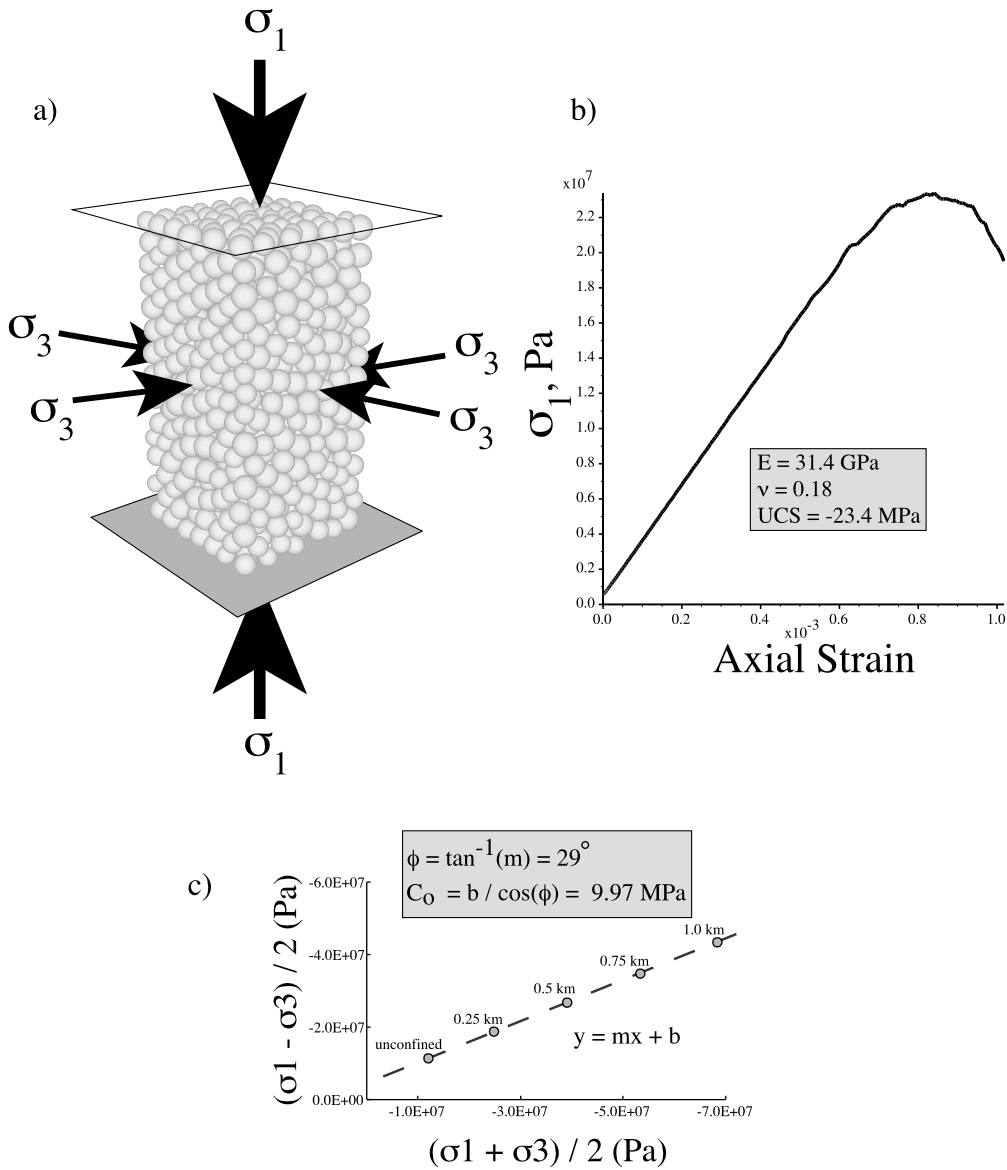
Fig. 2. Numerical biaxial test rig. (a) To determine the macro-scale rock mechanical properties, a representative sample of the numerical model is subjected to both unconfined and confined biaxial compression tests. (b) Unconfined test results yield: (1) Young's modulus (E) from the slope of the linear or elastic portion of the curve; (2) unconfined compressive strength (UCS) from the peak of the curve; and (3) Poisson's ratio (ν) from lateral strains (not shown here). (c) A linear regression through peak strength data plotted in shear-stress versus mean-stress space yields the angle of internal friction (ϕ) as the slope of the line and cohesion (C_o) as the y-intercept.

faults as a result of progressive bond breakage during shortening.

Because of the discrete, particle-based nature of the model, specification of material properties and boundary conditions is more difficult than with available continuum methods (Itasca, 1999a,b, 2000). The user may specify micro-properties that control particle–particle interaction (e.g. particle shear and bulk modulus, coefficient of friction, and bond strength), but has no way to directly prescribe the macro-properties of the model such as Young's modulus (E), unconfined compressive strength (UCS), cohesion (C_o), Poisson's ratio (ν), coefficient of friction (μ), porosity, and the initial stress state. As a result, the process of gener-

ating an initial model with the appropriate material behavior and initial stress state is by trial-and-error, requiring the use of the numerical equivalent of a biaxial rock mechanics test rig (Fig. 2) to derive the rock mechanical macro-properties.

The method employs a time-stepping, explicit-calculation scheme (Cundall and Strack, 1979), which has advantages over traditional implicit calculation schemes in that it can handle a large number of particles with modest memory requirements because there are no matrices to invert. Because the solution scheme solves the full dynamic equations of motion, dynamic propagation of waves through the bonded material occurs, simulating seismic waves whose velocities are dependent on the stiffness, density and
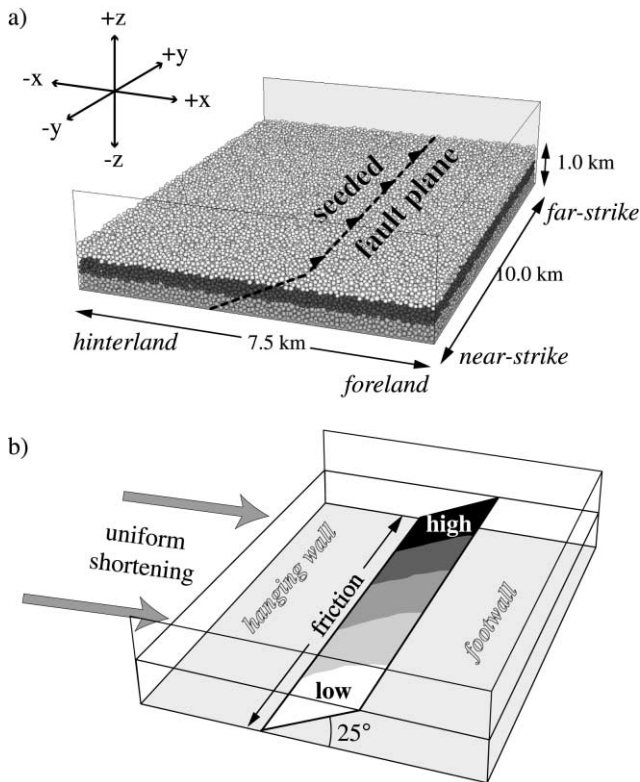
Fig. 3. Initial model configuration. (a) The initial numerical model consists of more than 83,000 spherical particles of variable size with a mean radius of 50 m. The granular aggregate is 1 km thick, 10 km wide in the strike direction and 7.5 km wide in the cross-strike or transport direction. Terminology for defining direction for the models is as follows: near-strike ($-y$) and far-strike ($+y$) are in reference to the viewer and represent the low and high friction ends of the fault, respectively. Hinterland ($-x$) and foreland ($+x$) directions are perpendicular to fault strike and parallel to the shortening direction. (b) A fault plane that dips 25° towards the hinterland is seeded within the assembly by setting the strength of bonds that cross the plane to an order of magnitude lower than the ambient particle bond strength. Friction is varied along the fault by modifying the frictional properties of contacts between particles that are on either side of the seeded fault plane. There are five rectangular fault patches with particle friction of $\mu = 0.0, 0.1, 0.2, 0.3$ and 0.4, from the near-strike to the far-strike direction, respectively.

packing of particles (Hazzard et al., 1998). This also allows physical instabilities such as shear-band formation to be modeled without numerical difficulty because kinetic energy that accompanies shear-band formation is released and dissipated in a physically realistic way (Itasca, 1999a).

2.3. Design and set-up of the 3D thrust ramp model

We use the following conventions to refer to directions in the model (Fig. 3a): the *model hinterland* is the back side of the model that is bound by the rear pushing wall ($-x$ direction). The *model foreland* is in the direction of shortening ($+x$ direction). *Near-strike* and *far-strike* refer to the $-y$ and $+y$ directions, respectively. We use the term *in-plane* to refer to material motion that is only in the x–z plane (the standard orientation of thrust-belt cross-sections and 2D

numerical models), and *out-of-plane* to refer to all motion that is not in the x–z plane.

The boundary conditions for the model were as simple as possible. The walls and base were elastic and frictional. The rear or hinterland wall advanced at a controlled, uniform velocity toward the foreland (right-hand side of Fig. 3). The upper surface of the model was free and the whole model was gravitationally loaded by 1 g.

The initial model geometry consisted of an open box with four side walls and a floor that contained the particles (Fig. 3a); the box measured 10 km in the along-strike direction, 7.5 km in the transport direction, and was 2 km high. The model material was composed of about 83,000 individual spherical particles whose average radius was 50 m. The ratio of largest to smallest particles was 1.33, with particle sizes varied about the mean in order to prevent hexagonal close-packing, which would produce three strongly preferred directions of faulting, rather than permitting fault orientations to be governed by local and applied stresses.

The initial model assembly was created by randomly placing more than 100,000 particles within the confining walls, and then allowing them to settle under the force of gravity. Once static equilibrium was achieved (defined here as when the unbalanced forces in the whole model assembly drop to a negligible value relative to the later applied force), the assembly was trimmed to the appropriate thickness by deleting particles above the specified 1.0 km elevation. Removing the upper particles resulted in a small amount of vertical elastic rebound, which elevated the upper surface of the assembly above 1.0 km. The model then was allowed to reach equilibrium and the trimming process was repeated until the desired thickness was obtained. Once the assembly had settled to equilibrium, normal and shear contact bonds were applied. The model assembly was divided up into three non-mechanical layers that served as passive markers. There was no bedding in the mechanical sense because particles were bonded across the layers (although such modifications have allowed study of effects of mechanical stratigraphy and bedding-plane slip in unpublished 2D models).

In the PFC3D software, *normal bonds* connect individual particles along a line between their centers and act to resist separation due to tension, and *shear bonds* act to resist tangential motion between particles. Once either the shear or normal bond strength is exceeded, the bond breaks, and the neighboring particles are free to move relative to each other with only frictional resistance between them. The plane of failure, or 'micro-fault', is the tangent surface at the point of contact at failure. In response to loading, throughgoing 'fault-zones' form by the coalescence of these individual micro-faults. 'Seismic' events are caused by individual bond breakage, with release of kinetic energy caused by elastic rebound of the two formerly bonded particles and their neighbors, and also due to slip between particles (Hazzard et al., 1998; Young et al., 2000). Friction between adjacent particles is active only when particles

are either unbonded, as during the initial gravitational settling, or after contact bonds have failed due to loading. The friction coefficient used in this study was $\mu = 0.577$ (30°), except where it was modified along the fault.

One way to force differential along-strike motion along a thrust fault is to apply a non-uniform shortening in the overall direction of tectonic transport, which causes faulting to initiate where the shortening is greatest. Alternately, we chose to apply uniform shortening to keep the boundary conditions and model relatively simple so that the results would be more easily interpretable. However, uniform shortening combined with parallel side walls has the effect of forcing uniform deformation along strike (e.g. Liu and Dixon, 1990). To force non-cylindrical motion along strike while maintaining uniform shortening, we had to either modify the footwall fault geometry along strike (Apotria, 1995) or to alter the along-strike mechanical properties (e.g. Liu and Dixon, 1991).

We chose to alter the fault strength by varying the along-strike friction of particles that lie on either side of the 'seeded' fault plane within the initial model (Fig. 3). In order to focus faulting and subsequent slip, we seeded a fault ramp that dipped 25° toward the hinterland and extended the full strike length of the model (Fig. 3a). Particle pairs whose centers lay above and below the fault plane had their contact bond strengths reduced to 10% of the ambient particle bond strength to force bond breakage along the fault. Friction on the seeded fault was everywhere less than the ambient particle friction ($\mu = 0.577$) and varied stepwise along strike. Five distinct patches, each about 2000 m in strike length, were assigned particle friction coefficients of $\mu = 0.0, 0.1, 0.2, 0.3,$ and 0.4, from the near-strike to far-strike direction, respectively (Fig. 3b). This forced slip to begin at the near-strike end of the model, at the zero friction patch, and to move steadily toward the higher friction end of the fault in the far-strike direction.

Seeding a fault has the disadvantage of making us force the location of faulting rather than letting the material fail on its own, which typically will not be in the center of the model because faults often nucleate at the boundary walls. In nature, this seeded fault might represent a weakly cemented, preexisting conjugate fracture or facies change. Along-strike friction variation might be due to lateral variation in weak sliding layers such as evaporite or coal (Verges et al., 1992), or to changes in cement or clay mineralogy. Thus, fault propagation here is identified as the along-strike rupture of the seeded fault plane and not an idealized fracture propagating though an unflawed, unbroken, homogeneous and isotropic rock mass. The fault tip is marked by the zero displacement loop that separates slipped and broken bonds from unslipped, still bonded parts of the seeded fault.

Because of the 2D boundary conditions imposed by the parallel sidewalls, out-of-plane displacements would likely be modest, but any out-of-plane motion observed at the center of the model would reflect the stresses and strains associated with 3D fault-related fold growth, and not the boundary conditions. In order to avoid the kinematic effects of the parallel side walls, we focused our observation on the center of the model. Furthermore, the majority of our along-strike displacement observations are from the lowermost layer of the model, because at depth the fault was better defined and the 'rock mass' was more intact.

2.4. Mechanical properties

In distinct-element models, we can only prescribe the mechanics of particle–particle, and particle–wall interactions by assigning the micro-mechanical properties of particle friction, contact bond strength, and force-displacement constants. As a result, there is no easy way to know a priori the macro-mechanical or rock mass mechanical properties of the model. We, therefore, performed numerical rock mechanics experiments on a representative particle aggregate to determine quantities such as Young's modulus (E), Poisson's ratio (ν), unconfined compressive strength (UCS), cohesion (C_o) and friction angle (ϕ), in order to determine that the model mechanical properties reasonably represented the mechanical response of a real rock mass. This was done using a numerical, servo-controlled, biaxial test-rig (Itasca, 1999b) to perform stress-strain experiments using specimens with the same packing, particle distribution, particle elastic properties, friction coefficient, and contact bond strengths as the full-scale model (Fig. 2a). Values of E, ν, and UCS were derived from uniaxial tests (Fig. 2b). C_o and ϕ were derived from a series of confined biaxial tests run at different confining pressures (Fig. 2c). The resultant rockmass macro-mechanical properties derived from these tests are provided in Fig. 2b and c.

One of the issues that must be addressed for these models is the question of scaling and particle size. The models are full scale, 1:1 with the natural world, and as such, there is no need to scale gravity. The mean particle radius of 50 m is determined by the limits of computational speed, but it nevertheless must function in the model as the characteristic size of intact blocks of rock. It is unlikely, however, that natural rocks in shallow-level fold-thrust belts are without discontinuities at this scale. For this reason, there might be an incentive to scale particle elastic moduli to account for discontinuities using methods drawn from rock mechanics literature such as the rock mass rating system (Bieniawski, 1989; Strayer et al., 1999b), but we did not attempt such a correction for this study. 2D and 3D numerical biaxial tests show that the mechanical response of specimens with half and twice as many particles are effectively identical, so long as there are enough particles to allow for localization and slip (Itasca, 1999a,b). Therefore, we assumed that there was independence between the
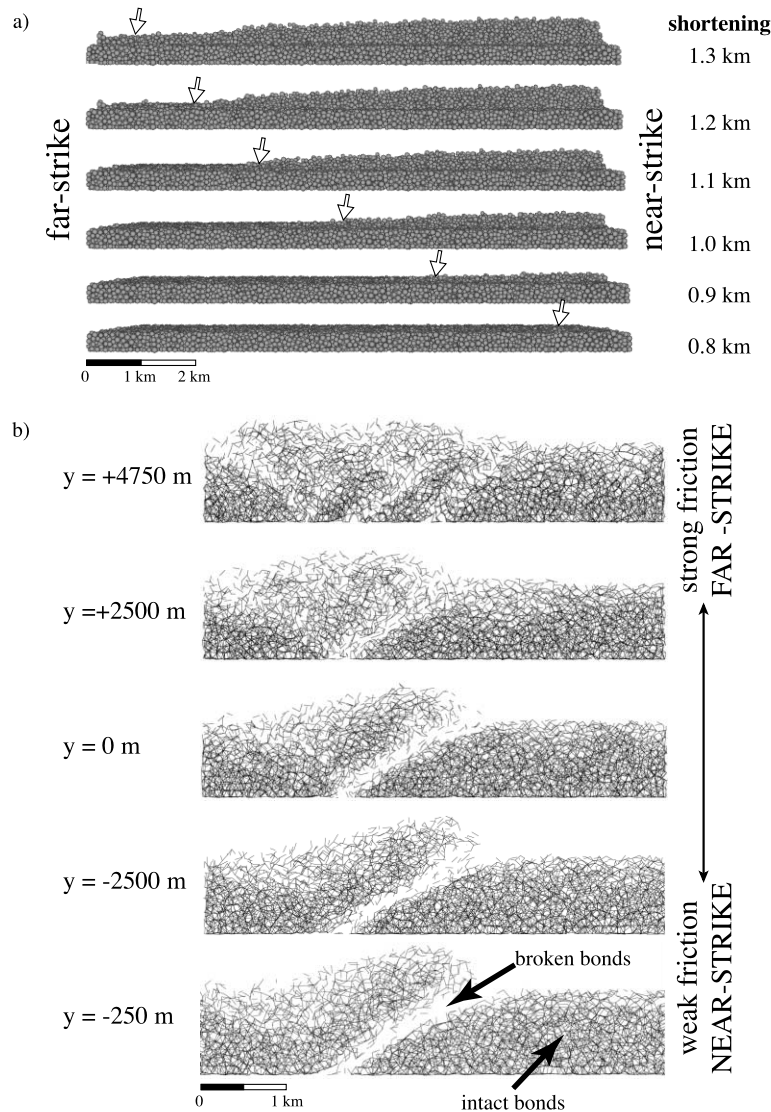
Fig. 4. Along-strike fault-related fold development. (a) Along-strike fold growth began first in Layer 1 and occurred rapidly after fault initiation at 0.8 km of shortening. The result was a well-developed, plunging anticline. Distributed faulting, not necessarily on the seeded fault, occurred at about 1.2 km shortening at the far-strike end of the model where fault friction was highest. (b) Along-strike variation of folding and faulting was represented by intact bonds at five locations along strike at 1.5 km shortening. Regions of broken bonds (faults) are represented by white areas. Each cross-section has different fault friction, resulting in progressively different styles of deformation. At low values of fault friction, deformation is accommodated almost entirely by slip on the fault and folding of the hanging wall, whereas high fault friction causes distributed back- and fore-thrusting in the hanging wall and footwall.

mechanical response of the model and the particle size in our experiments, while realizing that better discretization would likely allow smaller scale structures to form.

3. Results

3.1. General observations

The model was run until rear-wall displacement reached 1.5 km of the initial 7.5 km model. At about 1 km shortening, the fault had propagated steadily about 5 km along strike, and by 1.3 km shortening, the fault rupture had completely traversed the full 10 km strike length of the

model (Fig. 4a). If we assume model symmetry (i.e. the model represents half of an entire thrust fault), then the thrust displacement-to-length ratio was initially about $K = 10\%$, and later $K = 6.5\%$, which is in reasonably good agreement with Elliott's (1976) result of $K = 7\%$ based on natural faults (cf. Fermor, 1999). This observation must be tempered by the fact that this model possessed a fault with an inhomogeneous friction gradient and assumed that at the near-strike end of the model, all shortening was transferred into slip on the fault and not stored elastically. The most obvious feature of the model was a well-developed, non-cylindrical, fault-related fold that plunged towards the far-strike direction (Figs. 4 and 5). Because of the uniform-push boundary conditions, shortening had to be
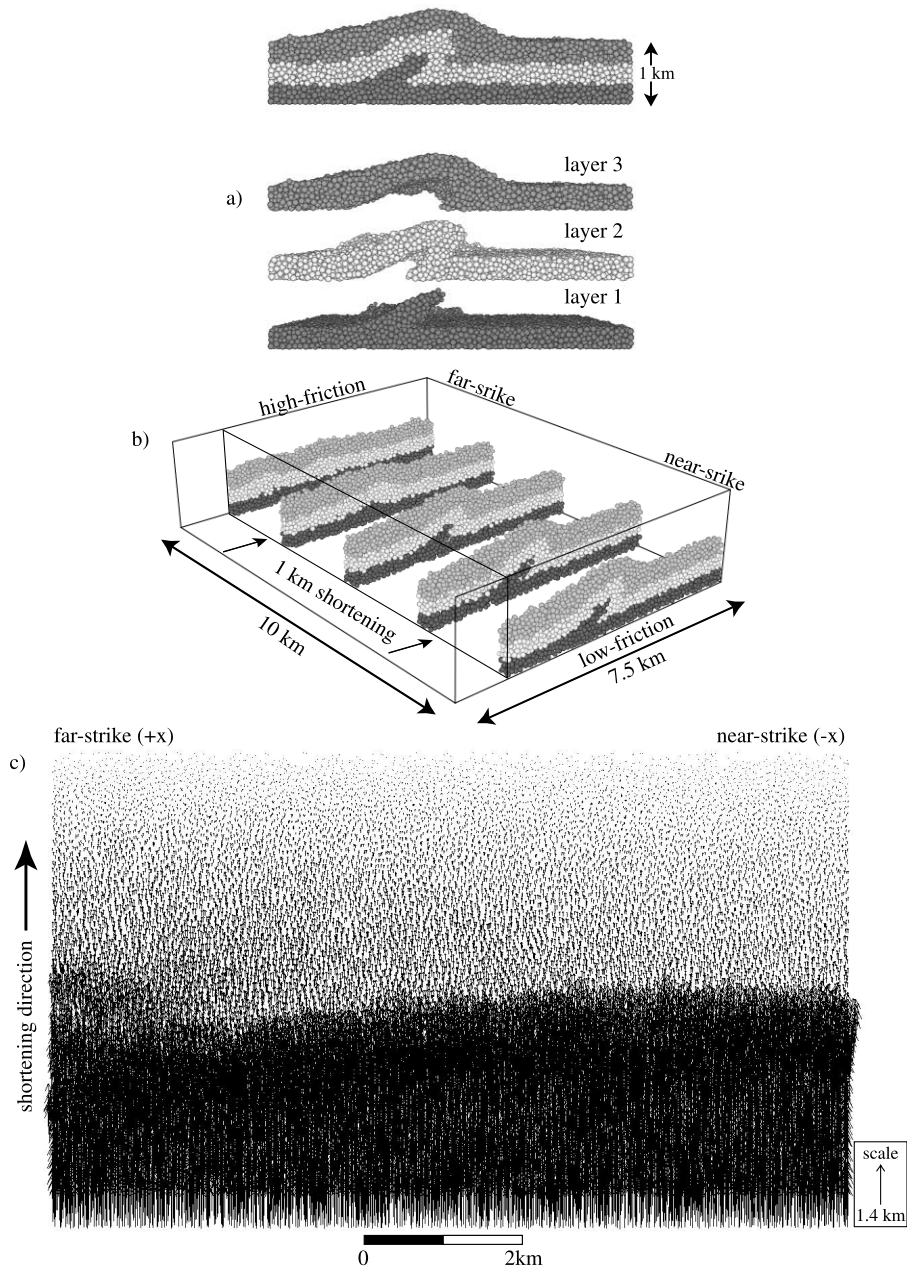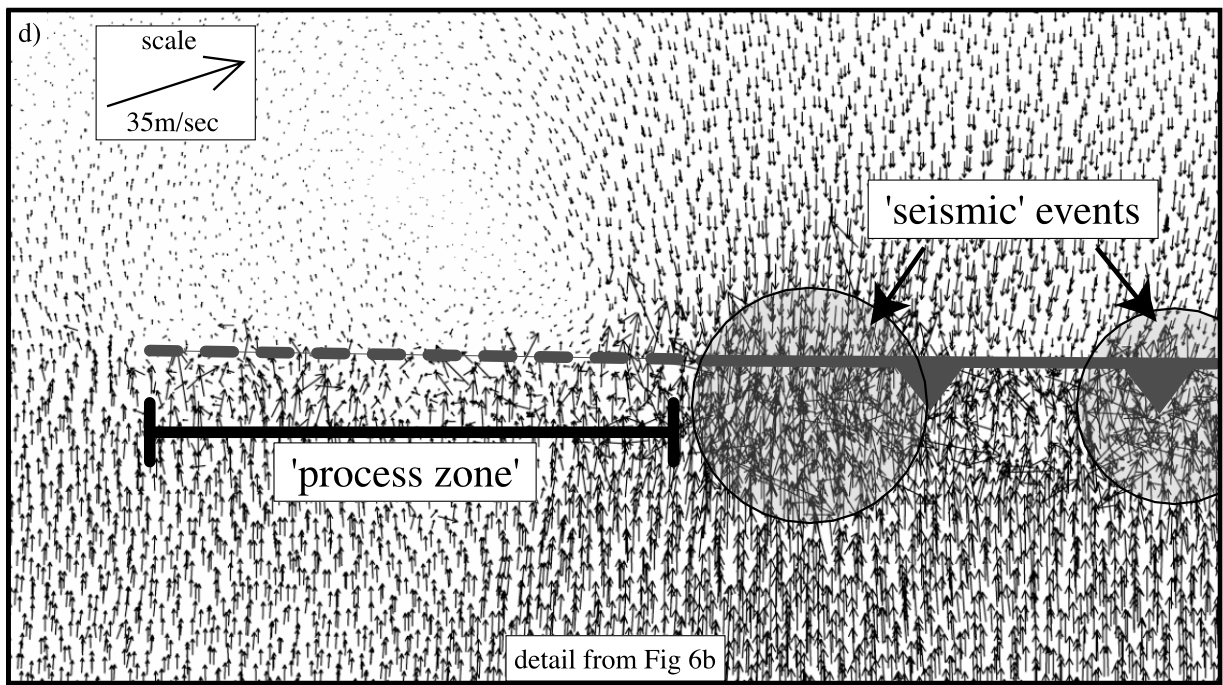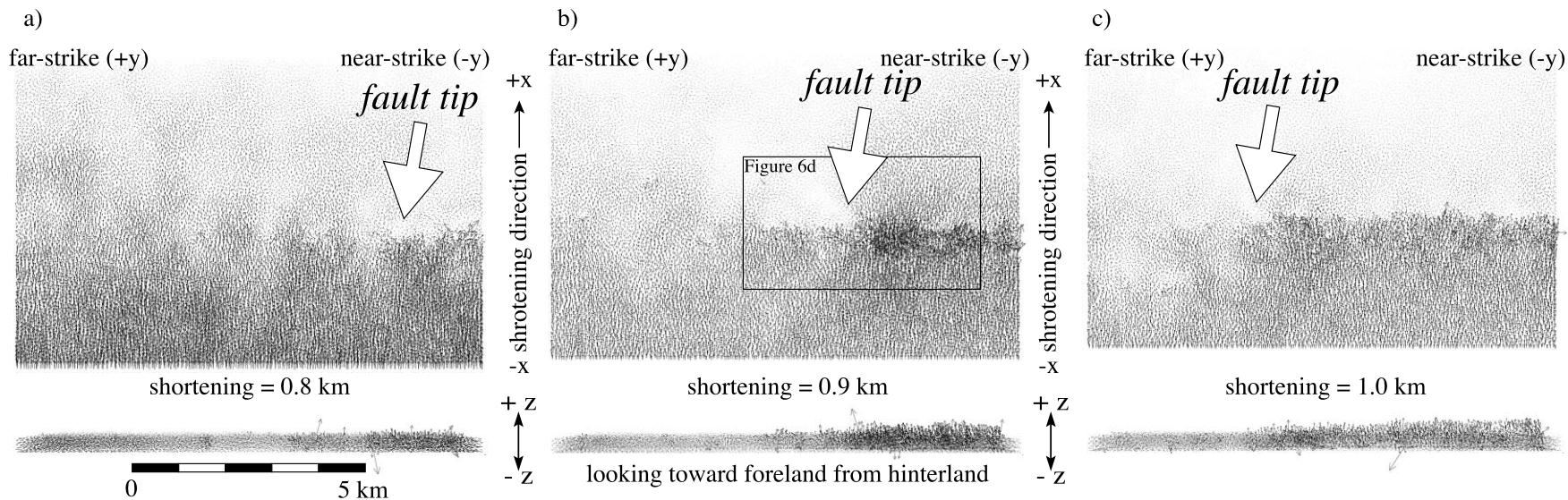
Fig. 5. General model that illustrates the development of a typical fault-related fold that progressively plunges out toward the far-strike direction. (a) Exploded view of the entire folded assembly showing non-cylindrical fold shape. Layers have no mechanical significance, and are only for ease of visualization. Faulting is discrete at depth and becomes more diffuse up-section with decreasing overburden. At the far-strike end where friction is highest, shortening is accommodated upon a series of unseeded or spontaneous faults, resulting in somewhat uniform shortening. (b) A fence diagram through the assembly shows the along-strike variation of fold development with uniform shortening resulting from varying fault friction along strike. (c) Displacement vectors in Layer 1 shows an arcuate trace of the thrust front, which dies out toward the far-strike end of the model with high fault friction. Displacement appears to be nearly all in the transport direction with little or no out-of-plane motion.

accommodated differently along strike. At the near-strike end, where fault friction was lowest, shortening was accommodated almost entirely by slip on the seeded fault, producing a well-developed ramp anticline. Backthrusting became more important as fault friction increased along strike. At the far-strike end where fault friction was just lower than the ambient model friction, shortening was accommodated by a series of conjugate back- and forward

thrusts that allowed the hanging wall to shorten by thickening without significant folding or use of the seeded fault (Fig. 4b).

The non-cylindrical nature of the structure is clearly seen in Fig. 5a and b. Each of the three passive layers shows distinct along-strike changes in geometry. The nature of localization on the fault changes with depth; the fault zone, initially only one or two particles thick, is sharp at

a)

far-strike (+y)　　　　near-strike (-y)

fault tip

+x

− shrotening direction →

−x

shortening = 0.8 km

+z

− z

0　　　　　5 km

b)

far-strike (+y)　　　　near-strike (-y)

fault tip

Figure 6d

+x

− shrotening direction →

−x

shortening = 0.9 km

+z

looking toward foreland from hinterland

− z

c)

far-strike (+y)　　　　near-strike (-y)

fault tip

shortening = 1.0 km

d)

scale

35m/sec

'seismic' events

'process zone'

detail from Fig 6b

depth and becomes diffuse higher up in the section as pressure due to overlying mass is reduced (Fig. 5a).

3.2. Out-of-plane motion

Because of boundary conditions and edge effects, any observation of out-of-plane motion that occurs during thrust slip and fold growth is likely to be most unaffected away from the model edges, toward the strike-center region of the model. As might be expected, incremental, single time-step particle motion represented by velocity vectors is somewhat 'noisy' when compared with the more regular pattern of displacement vectors, which integrate velocity and smooth out the sometimes irregular motion of individual particles moving past each other (Figs. 6 and 7). This 'noise' reflects the episodic or stick-slip nature of particle motion and fault slip during deformation. Incremental plots of single time steps often captures slip or 'seismic' events occurring at individual bonded contacts as the propagating fault tip moves through the particle assembly. This is illustrated in Fig. 6a–c, where a disturbance in the vector field can be seen migrating across-strike of the lowermost layer from the near-strike to the far-strike direction. The disturbance is manifest as a radially expanding shell of outward-directed velocity vectors whose source is a broken particle bond or frictional slip event. They represent seismic events (Young et al., 2000), with kinetic energy and magnitudes that depend on the velocity and mass of the material adjacent to, and involved in, the bond breakage or frictional-slip event.

There is a pronounced region of the footwall to the right and adjacent to the disturbed area, which is moving in the opposite or hinterland direction, effectively inserting itself under the hanging wall in Fig. 6d. This is a periodic response to horizontal elastic loading of the footwall that we often observe in these and in 2D simulations. In these models, both the hanging wall and footwall are elastically loaded in the direction of shortening during periods of fault 'stick'. When a portion of the fault slips, the hanging wall is transported over and past the footwall, while simultaneously the footwall elastically unloads (rebounds), and is inserted horizontally back to near it's initial position beneath the hanging wall. This general pattern of stick-slip elastic rebound is repeated throughout the simulation as fault slip occurs and the fold grows. Not all velocity vectors shown in Fig. 6 are parallel to the transport direction, showing that a component of incremental motion is out-of-plane. The distinct region of low particle velocity (light areas) in Fig. 6a–c effectively marks the fault tip. It separates the
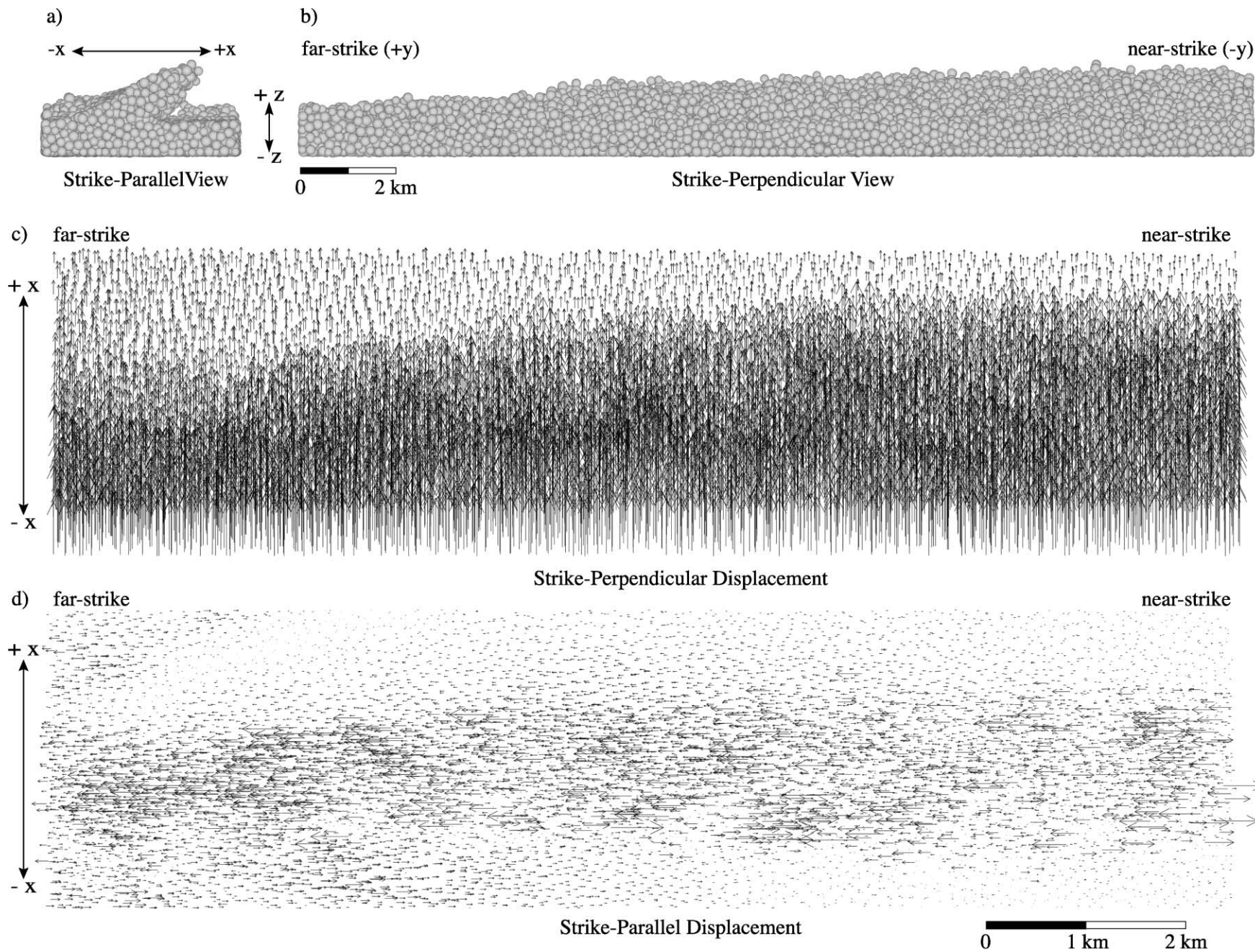
unfaulted part of the model that is still coupled across a not-yet-slipped part of the seeded fault, and is still in motion toward the foreland (Fig. 6d, left-side), from the footwall (Fig. 6d, upper-right).

In contrast to the velocity vectors, displacement vectors appear approximately parallel to the transport direction (Fig. 5c), which is expected given the boundary conditions. The displacement pattern in the hanging wall defines an arcuate fault trace with the maximum displacement at the near-strike (right) end of the model. In the lowermost layer (Layer 1), after the fault has fully propagated (1.5 km of shortening), we see a pattern of vectors that clearly distinguishes the hanging wall from the footwall, except at the far-strike (left) end of the model, where multiple faults distribute the shortening by thickening. Displacement in the footwall also appears to be in the transport direction, but dies out at the foreland model wall. Although there is some very limited permanent plastic strain in the footwall, this displacement is mostly the result of elastic loading.

In order to see any out-of-plane displacements that may be present, we decomposed the individual displacement vectors into their three (x, y, z) components (Figs. 2a and 7c and d), focusing specifically on the x and y components that are parallel to the transport and strike directions, respectively. Again, focusing on the lowermost layer, in a 2-km-wide strike-parallel region (Fig. 7a and b), the x component of displacement has a mean of $+749$ m and a maximum value of $+1401$ m at about 1.5 km of total shortening. In the same region, the maximum strike-parallel (or y) component of the displacement vectors has a mean displacement of 8.22 ± 0.53 m in the plunge direction (95% large-sample confidence interval), and ranges between $+274$ and -209 m (standard deviation of 29.11 and $n = 11539$; Fig. 8). Focusing now on only the y component of displacement, and separating the far-strike ($+y$, left in Fig. 7d) from the near-strike ($-y$, right in Fig. 7d) directed vectors, the far-strike-directed displacement has a maximum of $+274$ m, with a mean of $+21$ m. The maximum near-strike-directed displacement is -209 m with a mean of -18 m (Fig. 8). Casual inspection of Fig. 7d suggests that the majority of the along-strike displacement vectors are far-strike-directed (toward the left). In fact, out of 11,539 particles considered in this analysis, about two-thirds (7783) of the particles moved in the far-strike direction, and about one-third (3756) moved towards the near-strike direction.

Looking in more detail at a representative area of the strike-parallel (y direction) displacement vectors (Fig. 9), again it appears that many of the vectors are far-strike-directed ($+y$, toward the fault-propagation and fold-plunge

Fig. 6. Velocity vectors in Layer 1. In map-view (a–c), velocity vectors in Layer 1 show the along-strike propagation of the fault and location of the fault tip, represented by a white patch indicating low particle velocity. The area of the fault tip in (b) is shown in detail in (d). The low velocity (white) patch separates parts of the model where the footwall is being inserted beneath the hanging wall during fault slip (right), from where the fault has not yet completely traversed the whole model and the footwall is still in motion toward the foreland. Shaded circles are centered on 'seismic' events; that is, disturbances in the velocity field caused by either fault rupture or slip. Each disturbance is composed of a spherical group of velocity vectors representing sound waves that radiate out from the bond breakage or particle slip event.

a)

−x ←——→ +x

+ z
− z

Strike-ParallelView

b)

far-strike (+y)

near-strike (−y)

Strike-Perpendicular View

0   2 km

c)   far-strike

near-strike

+ x

− x

Strike-Perpendicular Displacement

d)   far-strike

near-strike

+ x

− x

Strike-Parallel Displacement

0   1 km   2 km

direction), but note that there are also a number of small regions where groups of particles have opposite, near-strike-directed motion. These regions are separated by what are perhaps the distinct-element equivalents of small-scale, bedding-normal, strike-slip faults that are active transiently, and are sometimes conjugate. They accommodate shortening parallel to transport, and result in along-strike extension as in natural fold systems. This likely occurs in concert with transient thickening in other parts of the model because actual along-strike extension is impossible with the boundary conditions.

We have not explicitly determined if there is any rotation of the hanging wall about a vertical axis, but there appears to be no evidence for it from the pattern of strike-perpendicular displacement vectors (i.e. longer vectors at the right end of Fig. 7c). Given the boundary conditions, however, this should come as no surprise.

To summarize, there is a statistically significant degree of material motion in the direction of thrust-fault propagation and fold plunge. We see out-of-plane displacements that are an order of magnitude or two less than in-plane displacements. The displacements appear to be the result of strike-parallel extension, and occur upon transiently active, sometimes conjugate, bedding-perpendicular fault zones. Permanent along-strike extension, however, is at odds with the fixed-side boundaries, and therefore, the bedding-perpendicular faults must balance to yield no net extension, perhaps in conjunction with vertical thickening and/or growing fold topography.

4. Discussion and conclusions

We have constructed a numerical 'sandbox' model of a growing fault-related fold with bonded particles with relatively simple initial and boundary conditions. The only three-dimensionality comes from an along-strike gradient in friction on the thrust ramp. From this, we hoped to gain a first-order understanding of the nature and magnitude of out-of-plane material movement during thrusting caused solely by fault heterogeneity. The modeling showed a systematic, but modest along-strike motion in the direction of increasing friction. In contrast, early simulations without a friction gradient produced a cylindrical fault-related fold with effectively identical cross-sections along strike and with no statistical 'asymmetry' (Fig. 8) to the finite strike-parallel motion. Instead the near-strike and far-strike displacements effectively balance, resulting in a mean of zero. Thus, some form of systematic 3D heterogeneity seems to be required to induce systematic 3D motion; other mechan-

isms that we did not include in this initial exploration that would probably lead to 3D motion include truly 3D displacement boundary conditions and more heterogeneous fault nucleation with extensive displacement transfer.

Along-strike variation of fault friction combined with uniform shortening produced a well-developed, non-cylindrical, plunging fault-related fold. The deformational style of the structure changed distinctly along strike, which must be a product of differences in along-strike fault friction, and is not consistent with the notion of along-strike spatial and temporal similarity (e.g. Poblet et al., 1998). This is not surprising, but it serves to remind us that this convenient and powerful notion of spatial and temporal geometric equivalence may not be satisfied in detail in natural systems because the associated mechanical requirements may be difficult to realize naturally.

Along-strike fault propagation was rapid once initiated. The fault had displacement-to-length ratios that decreased from an initial value of $K = 10\%$ to $K = 6.5\%$ once the fault tip had traversed the model, which is consistent with natural fault systems (Elliott, 1976; Fermor, 1999). These displacement-to-length ratios yield displacement gradients of 0.2 and 0.13, respectively. Displacement gradients can vary widely within a single thrust sheet (Wilkerson, 1992; Fermor, 1999), implying that the length of a thrust fault is not linearly related to displacement as initially suggested by Elliott (1976). The varying displacement gradients in our models are likely the result of inhomogeneous along-strike fault friction. In natural thrust systems, it is not unreasonable to assume that the non-linear displacement-to-fault-length ratios of Fermor (1999) may be a function of natural variation in along-strike fault and stratigraphic mechanical properties as well as along-strike topographic differences, which affect the stress state at depth.

Fault propagation and fold growth occur in an episodic, stick-slip manner in the model as seen in plots of particle velocities. During periods of fault 'stick' the whole particle assembly was elastically loaded and displaced toward the foreland. Slip events were marked by 'seismicity' originating at the fault tip and also along the fault plane. During slip the hanging wall moved episodically toward the foreland, and the footwall was concurrently inserted back beneath the hanging wall by elastic unloading or rebound. This repeated horizontal loading and rebounding of the footwall that was evident in these and unpublished 2D models perhaps addresses the observation in thrust belts that the footwall rocks tend to be more deformed than the adjacent hanging wall rocks (Evans and Neves, 1992).

Along-strike, out-of-plane material displacement is an order of magnitude or two less than in-plane displacement.

Fig. 7. A 2-km-wide swath of particles from the lowermost layer for displacement analysis (a, b). (c) Strike-perpendicular (*x*-direction) component of particle-displacement vectors in map-view shows the displacement of the hanging wall in Layer 1. (d) Strike-parallel (*y*-direction) displacements in map-view are an order of magnitude or two less than in-plane displacements and appear to be generally far-strike-directed. However, a significant number of particles have been transported in the opposite direction.
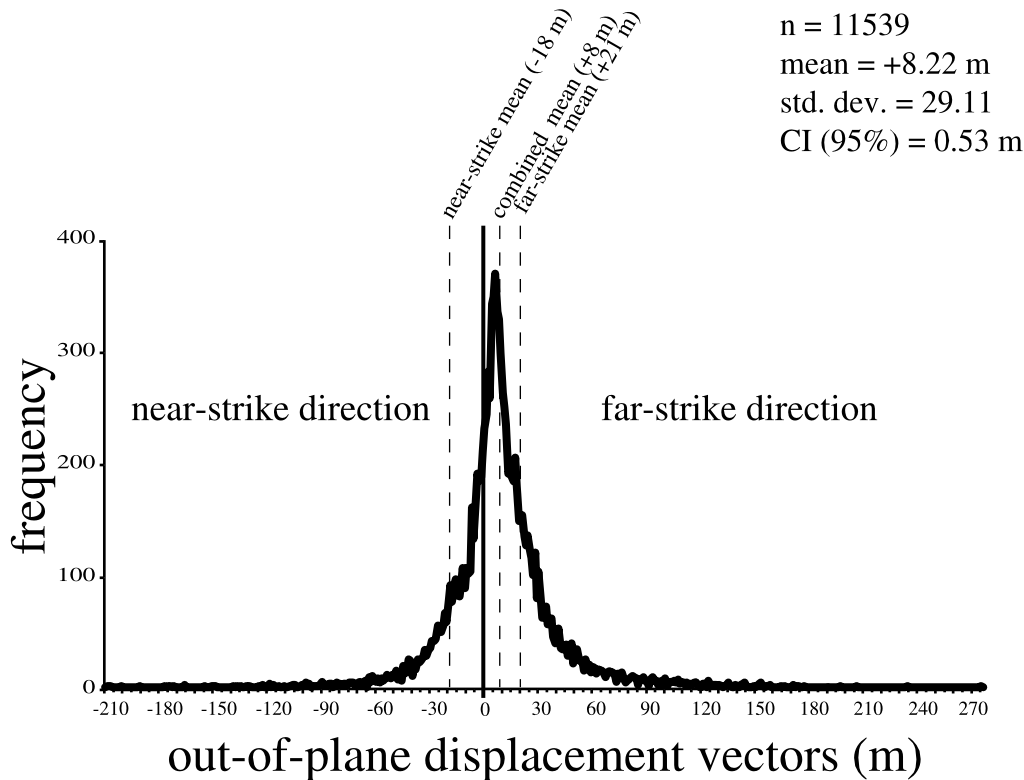
Fig. 8. Histogram of strike-parallel (*y*-direction) displacement vectors (*n* = 11,539). The population mean is +8.22 m (far-strike-directed) with a large population 95% confidence interval of 0.53 m. The separate means for the far-strike (+*y*) and near-strike (−*y*) displacement vectors are +21 m and −18 m, respectively.

There is an apparent and statistically robust pattern of along-strike displacement in the direction of fault propagation. The out-of-plane displacement varies locally, caused by the formation of small-scale 'blocks' of bonded particles that are separated by bedding-perpendicular, apparently conjugate, strike-slip fault sets, resulting in strike-parallel extension in response to thickening of the hanging wall. The appearance of motion generally in the direction of fault propagation also may be topographically induced. The emergent anticline plunges consistently in the direction of fault propagation, and this should have the effect of imparting a shear traction in that direction to all particles below the topographic expression of the fold.

The validity of these model results for natural structures is a direct function of the assumptions and simplifications that we make in building the model and their correspondence to natural systems. For example, are the boundary and initial conditions realistic? Are the mechanical properties of the rock mass appropriate? How well does a distinct-element approach such as that used by PFC3D simulate pressure-dependent, brittle-plastic deformation in a thrust system? Our model does not attempt to simulate the important vagaries of any specific thrust ramp. It is, however, a reasonable representation of a kilometer-scale thrust and attendant fold, that is fully dynamic, uses realistic pressure-dependent rock material properties (Fig. 2), and reproduces a number of features seen in natural thrust systems. In particular, these models illustrate the extent to which gradients in fault-ramp friction can induce along-strike motion.

The rules of thumb resulting from this work that may be of use to a field geologist are: (1) maximum along-strike material motion might be as much as 10% of the strike-perpendicular motion. This motion may be represented by strike-perpendicular stylolites or other micro-structures that suggest the presence of along-strike stresses. However, mean along-strike motion may be only about 1% of regional shortening, and as such may be difficult to detect in the field; (2) this motion occurs upon bedding-perpendicular, strike-oblique, perhaps conjugate fractures that are commonly seen in thrust belts; and, (3) that we should be vigilant for indicators of systematic top-to-the-plunge-direction, along-strike bedding-parallel shear. Their presence may suggest that topographic slope may be driving the general pattern of along-strike, plunge-directed, material motion seen in these models.

Acknowledgements

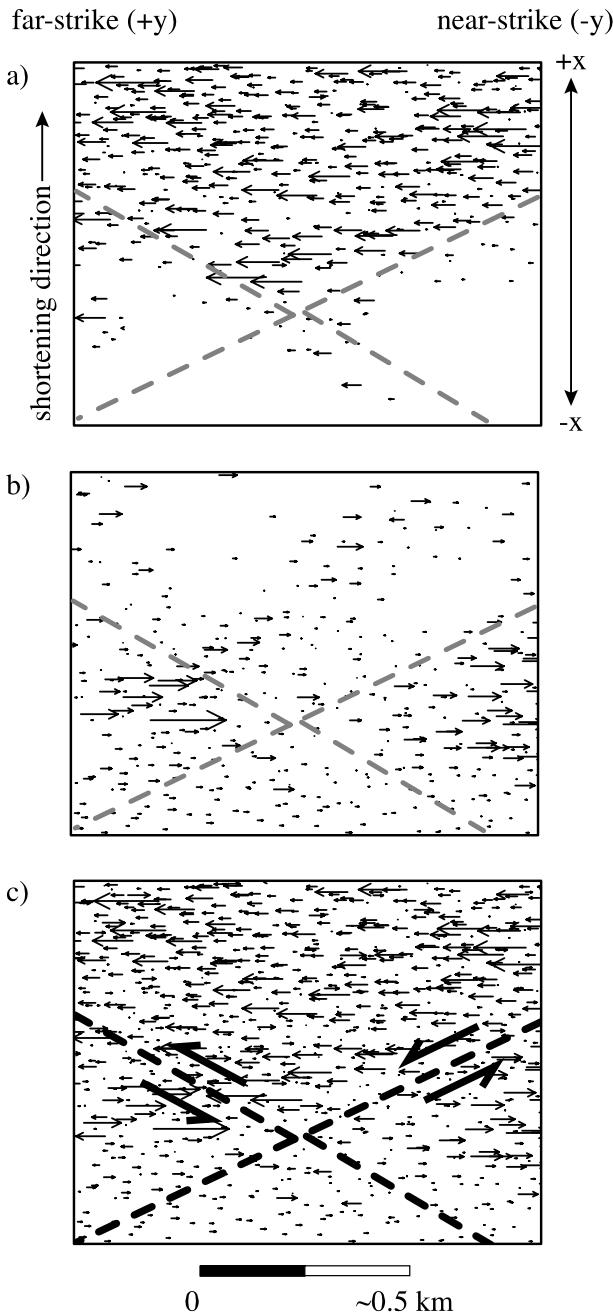far-strike (+y)   near-strike (-y)

Fig. 9. Detail of along-strike displacement from a 1 km² representative area of Fig. 7d. (a) Far-strike (+y) -directed vectors only. (b) Near-strike (−y) -directed vectors only. (c) Combined far- and near-strike-directed vectors suggest there are clusters of particles moving systematically in either strike-parallel direction, separated by bedding-perpendicular fault zones (dashed lines), which are active transiently throughout the simulation.

References

Allmendinger, R.W., 1998. Inverse and forward numerical modeling of trishear fault-propagation folds. Tectonics 17, 640–656.

Apotria, T.G., 1995. Thrust sheet rotation and out-of-plane strains associated with oblique ramps: an example from the Wyoming salient, USA. Journal of Structural Geology. 17, 647–662.

Bieniawski, Z.T., 1989. Engineering Rock Mass Classifications. John Wiley & Sons, New York.

Bilotti, F.D., Shaw, J.H., Brennan, P.A., Connors, C.D., Prelat, A.E., 1998. Integrated remote sensing and structural geology to define complex fold-and-thrust belt structures. American Association of Petroleum Geologists Bulletin Abstracts 82 (10), 1893.

Cristallini, E.O., Allmendinger, R.W., 1999. Pseudo-3D numerical analysis of the trishear fault-propagation fold model. Geological Society of America Abstracts with Programs 31, 127.

Cundall, P.A., 1988. Computer simulations of dense sphere assemblies. In: Satake, M., Jenkins, J.T. (Eds.). Micromechanics of Granular Materials, pp. 113–123 Studies in Applied Mechanics 20.

Cundall, P.A., 2001. A discontinuous future for numerical modelling in geomechanics? Geotechnical Engineering 149, 41–47.

Cundall, P.A., Strack, O.D.L., 1979. A discrete numerical model for granular assemblies. Geotechnique 29, 47–65.

Dahlstrom, C.D.A., 1969. Balanced cross-sections. Canadian Journal of Earth Sciences 6 (1), 743–757.

Dixon, J.M., Liu, S., 1992. Centrifuge modelling of the propagation of thrust faults. In: McClay, K.R. (Ed.). Thrust Tectonics. Chapman & Hall, London, p. 1.

Dixon, J., Spratt, D., 1999. 3D geometry and kinematics near tear faults and lateral ramps. In: K.R. McClay (Ed.), Thrust Tectonics, in press.

Elliott, D., 1976. The motion of thrust sheets. Journal of Geophysical Research 81, 949–963.

Erickson, S.G., 1995. Mechanics of triangle zones and passive-roof duplexes: implications of finite-element models. Tectonophysics 245 (1–2), 1–11.

Erickson, S.G., Jamison, W.R., 1995. Viscous-plastic finite-element models of fault-bend folds. Journal of Structural Geology 17, 561–573.

Evans, J.P., Neves, D.S., 1992. Footwall deformation along the Willard Thrust, Sevier orogenic belt: implications for mechanisms, timing, and kinematics. Geological Society of America Bulletin 104, 516–527.

Fermor, P., 1999. Aspects of the three-dimensional structure of the Alberta Foothills and Front Ranges. Geological Society of America Bulletin 111, 317–346.

Finch, E., McCloskey, J., 1996. Characteristic displacements of normal faults in a discrete element model of crustal extension. Eos, Transactions, American Geophysical Union 77 (46), 504.

Hazzard, J.F., Maxwell, S.C., Young, R.P., 1998. Micro-mechanical modelling of acoustic emissions. Society of Petroleum Engineers, SPE, 47320.

Itasca, 1999a. Particle Flow Code in 2 Dimensions — Users Manual. Itasca Consulting Group, Minneapolis, MN, USA.

Itasca, 1999b. Particle Flow Code in 3 Dimensions — Users Manual. Itasca Consulting Group, Minneapolis, MN, USA.

Itasca, 2000. Fast Lagrangian Analysis of Continua — Users Manual. Itasca Consulting Group, Minneapolis, MN, USA.

Liu, S., Dixon, J.M., 1990. Localization of thrust ramps by buckling: analog and numerical models. Geological Society of America Abstracts with Programs 22 (7), 141.

Liu, S., Dixon, J.M., 1991. Centrifuge modelling of thrust faulting: structural variation along strike in fold-thrust belts. In: Cobbold P.R. (Ed.), Experimental and Numerical Modelling of Continental Deformation. Tectonophysics 188(1–2), 39–62.

Morgan, J.K., 1998. The micro-mechanics of localization and dilation in granular shear zones revealed by distinct element simulations. Eos, Transactions, American Geophysical Union 79 (17), 222.

Poblet, J., Munoz, J.P., Trave, A., Serra, J.K., 1998. Quantifying the

kinematics of detachment folds using three-dimensional geometry: application to the Mediano Anticline (Pyrenees, Spain). Geological Society of America Bulletin 110, 111–125.

Potyondy, D.O., Cundall, P.A., Lee, C., 1996. Modeling rock using bonded assemblies of circular particles. In: Rock Mechanics Tool and Techniques, Proceedings of Second North American Rock Mechanics Symposium, Montréal, Canada, pp. 1937–1944.

Rouby, D., Xiao, H., Suppe, J., 2000. 3D restoration of complexly folded and faulted surfaces using multiple unfolding mechanisms. American Association of Petroleum Geologists Bulletin 84, 805–829.

Rowen, M.G., Linares, R., 2000. Fold-evolution matrices and axial-surface analysis of fault-bend folds: application to the Medina Anticline, Eastern Cordillera, Columbia. American Association of Petroleum Geologists Bulletin 84, 741–764.

Saltzer, S.D., Pollard, D., 1991. Mechanically based numerical modeling of structures formed during crustal extension and in sandbox experiments. Eos, Transactions, American Geophysical Union 72 (17), 271.

Shaw, J.H., Hook, S.C., Suppe, J., 1994. Structural trend analysis by axial surface mapping. American Association of Petroleum Geologists Bulletin 78, 700–721.

Stockwell, C.H., 1950. The use of plunge in the construction of cross-sections of folds. Proceedings of the Geological Association of Canada 3, 97–121.

Strayer, L.M., Hudleston, P.J., 1997. Numerical modeling of fold initiation at thrust ramps. In: Anastasio, D.J., Erslev, E.A., Fisher, D.M., Evans, J.P. (Eds.), Special Issue on Fault-Related Folding, Journal of Structural Geology 19(3–4), 551–566.

Strayer, L.M., Hudleston, P.J., 1997b. Simultaneous folding and faulting and fold-thrust belt evolution: a distinct-element model. Geological Society of America Abstracts with Programs 29 (6), 44.

Strayer, L.M., Erickson, S.G., Suppe, J., 1999a. Influence of growth-strata on the evolution of fault-related folds: distinct element models. Geological Society of America Abstracts with Programs 31, 237.

Strayer, L.M., S.G. Erickson, J. Suppe, 1999. Influence of growth-strata on the evolution of fault-related folds: distinct element models. In: K.R. McClay (Ed.), Thrust Tectonics, in press.

Verges, J., Munoz, J.A., Martinez, A., 1992. South Pyrenean fold-and-thrust belt: role of foreland evaporitic levels in thrust geometry. In: McClay, K.R. (Ed.). Thrust Tectonics. Chapman & Hall, London, p. 1.

Wilkerson, M.S., 1992. Differential transport and continuity of thrust sheets. Journal of Structural Geology 14, 749–751.

Wilkerson, M.S., Medwedeff, D.A., Marshak, S., 1991. Geometrical modeling of fault-related folds: a pseudo-three-dimensional approach. Journal of Structural Geology 13, 801–812.

Young, R.P., Hazzard, J.F., Pettitt, W.S., 2000. Seismic and micro-mechanical studies of rock fracture. Geophysical Research Letters 27, 1667–1670.